Proceedings of the 21st ICSMGE, Vienna, Austria, 14 – 19 June 2026. Pistrol, Adam & Schweiger (eds.)
Published by: ÖGG, Austrian Society for Geomechanics, Salzburg, Austria, ISBN 978-3-9503898-4-5
https://doi.org/10.53243/ICSMGE2026-2007

An early warning system for weather-induced landslide activity in clayey slopes: a novel stability chart for deep sliding bodies

Vito Tagarelli, Federica Cotecchia
Department of Civil, Environmental, Land, Construction and Chemistry, Polytechnic University of Bari, Italia,
vito.tagarelli@poliba.it

ABSTRACT: Based upon both phenomenological and numerical analyses, current landslide activity in clayey slopes is recurrently triggered by the soil-vegetation-atmosphere interaction taking place in the very topsoil layers. This interaction can cause transient seepage down to large depths in the slope, resulting in significant variations of pore water pressures and available strength with time at both shallow and large depths below the water table, i.e. variation of the slope equilibrium, defined as slope-vegetation-atmosphere interaction. Such interaction is found to trigger the activity of either shallow landslides or deep slow landslide bodies in clayey soils. This contribution reports insights into both the pore water pressure and the safety factor variations determined by the soil-vegetation-atmosphere interaction at the ground surface of slopes made of clayey turbidites, location of seasonal acceleration of deep landslide displacements and also shallow landsliding. The analyses are carried out by referring to a representative slope and are validated against field data. The results of the numerical analyses are shown to succeed in reproducing the current weather-induced activity of the landslide bodies so that the adopted modelling represents a tool to be used within early warning systems for the mitigation of the landslide risk in the slope scenarios of reference. Finally, a stability chart is proposed as a tool for the early warning related to deep sliding bodies in clayey turbidites, by making use of weather precursors relating to the 180-day cumulative rainfall, found to be connected to the landside activity.

KEYWORDS: Weather-induced landslides; Soil–vegetation–atmosphere interaction; Landslide early warning system.

1 INTRODUCTION

The stability of slopes is strongly influenced by soil–vegetation–atmosphere, SVA, interaction, which couple thermodynamic, hydraulic, and mechanical processes and involve exchanges of water, air, and heat between soil, vegetation, and the atmosphere (Gens, 2010). This interaction is governed by weather variables (rainfall, radiation, humidity, wind, temperature), vegetation traits, surface morphology, and soil hydro-mechanical behavior. SVA processes affect soil saturation, pore pressures, and straining in the topsoil, thus influencing overall slope stability (Cotecchia et al., 2019; Cecconi et al., 2025).

Research on modeling and interpreting SVA effects on landslides has grown over recent decades, supported by advances in monitoring techniques and understanding of thermo-hydro-mechanical behavior in partially saturated soils (e.g. Oorthuis et al., 2018; Tagarelli & Cotecchia, 2022). Deterministic models now combine field monitoring with numerical simulations, improving predictions of slope behavior and enabling their integration into landslide early warning systems, LEWS. Such systems traditionally rely on displacement thresholds to trigger alerts, but incorporating SVA-driven indicators (e.g., piezometric head, suction, water content, e.g., Rianna et al., 2023) and weather precursors allows earlier warnings and more effective risk mitigation.

Most deterministic LEWS have been only applied to shallow landslides (Salciarini et al., 2012), often using simplified infinite slope models, while regional-scale systems rely on empirical or statistical approaches (Calvello et al., 2015; Gariano et al., 2015). This paper proposes a methodology for uncoupled hydro-mechanical numerical modeling that predicts piezometric conditions and factor of safety (FS) in real-time for any slope, linking FS $\leq$ 1 to landslide acceleration. Once validated against field data, this approach can be integrated into site-scale LEWS and used to characterize weather precursors of landslide activity by running simulations over large weather datasets.

The methodology is applied to the Pisciolo slope in the southern Apennines (Italy), a complex geological-hydro-mechanical context with fissured clayey turbidites and fractured interbeds, where high piezometric heads and seasonal fluctuations predispose slopes to deep landslides reactivation. The study demonstrates how the approach can support site-specific LEWS design and improve understanding of how landslide indicators and weather precursors vary with depth.

This contribution adopts an uncoupled hydraulic-limit equilibrium, H–LE, modelling strategy to analyze the effects of the slope-vegetation-atmosphere, SLVA, interaction on slope stability, offering a computationally lighter alternative to fully coupled THM models (Elia et al., 2017). The approach combines: i) hydraulic, H analysis, which solves the Richards equation across a finite element slope model to simulate transient seepage driven by net rainfall (precipitation minus runoff, evaporation, and transpiration, estimated via the FAO Penman–Monteith method, Allen et al., 1998); ii) limit equilibrium (LE) analysis which computes the time-dependent factor of safety (SF) for selected landslide bodies, with SF $\leq$ 1 indicating potential acceleration or reactivation.

The adopted workflow involves the construction of a geo-hydro-mechanical, GHM, model of the slope, estimating surface fluxes, running and validating hydraulic analyses against field piezometric data, and then integrating results into LE stability analyses (Tagarelli & Cotecchia, 2025).

This methodology predicts the evolution of piezometric heads and SF over time, providing real-time indicators of landslide activity that can be integrated into site-specific LEWS. It also allows the identification of weather precursors and thresholds for landslide acceleration through simulations under varying meteorological conditions.

2 THE PROTOTYPE SLOPE AND LANDSLIDE ACTIVITY: THE PISCIOLO SLOPE

This research activity focuses on the Pisciolo slope in the south-eastern Apennines, representative of complex clayey slopes formed by fissured high-plasticity clays (Paola Doce and Red Flysch units) interbedded with coarse layers and fractured rock. These geological features give the slope higher field-scale permeability than typical for intact clays, allowing deep (up to 50–60 m) and seasonally fluctuating pore water pressures, closely correlated with 180-day cumulative rainfall.

In such GHM scenario, pore-water pressure variations in clayey slopes, extending to depths of 50–60 m, are strongly linked to seasonal fluctuations of the 180-day cumulative rainfall. Pore water pressures rise from early–mid autumn to early spring, peaking together with rainfall, and decline through late spring and summer. Medium- to deep-seated slow-moving landslides (Cruden & Varnes, 1996) respond with mild accelerations in winter, reaching maximum displacement rates in late winter–early spring, and decelerating in summer.

The Pisciolo slope, thoroughly investigated by Cotecchia et al. (2014) is representative of this GHM context. It is mainly composed of high-plasticity fissured Paola Doce clays (PD), interbedded with fractured rock and overlying higher-plasticity scaly Red Flysch clays (RF), deformed by an anticline structure. Despite their plasticity, fissuring and permeable interbeds yield $k_s \approx 10^{-9}$ m/s (Pedone et al., 2022a). PD clays exhibit dilative behaviour and peak friction angles of 16.1°–25.3° (avg.≈20.7°), dropping to 13°–18° post-peak (Cotecchia et al., 2014).

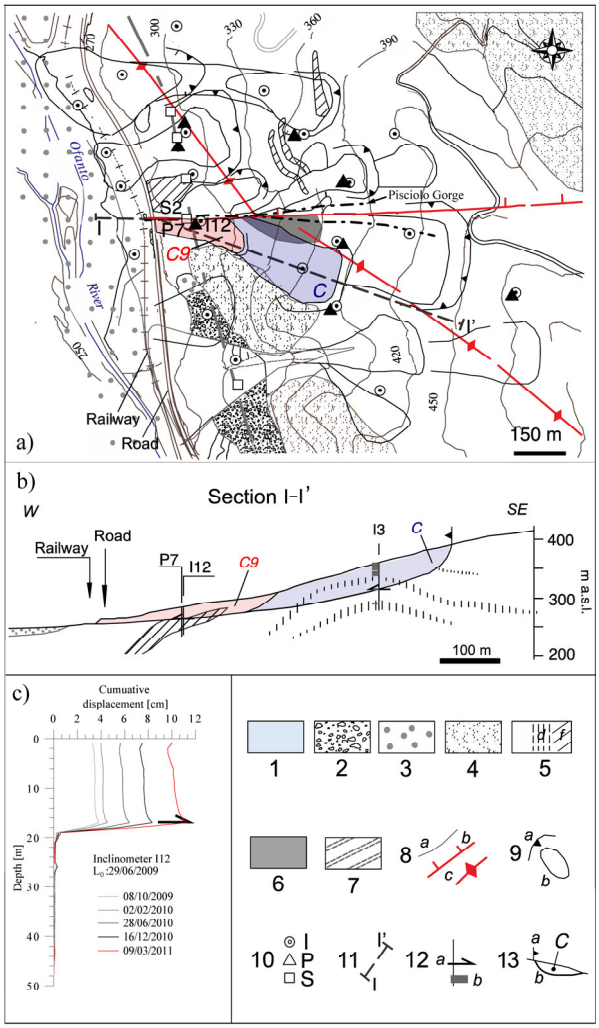

Figure 1. Geological map (a) and section (b) of the Pisciolo slope, inclinometer monitoring data, I12 (c), modified from Cotecchia et al., (2014, 2015). Key: 1, fan deposit; 2, debris; 3, alluvial deposit; 4, N sandstones; 5, PD clays with (d) disarranged rock, (f) locally fractured rock; 6, RF clays with rock/coarse-grained; 7, soil slips; 8, stratigraphic contact (a), fault (b), anticline axis (c); 9, landslide: crown (a), body (b); 10, boreholes with piezometers (P), or inclinometers (I), or GPS sensors (S) (only labels of the boreholes mentioned in the paper are reported); 10, trace of the section shown in frame (b); 12, inclinometer shear bending (a), remoulded soil core (b); 13, landslide: crown (a) and slip surface (b).

Monitoring revealed highest activity on the south side of the Pisciolo stream, with a shear band at 19 m depth (inclinometer I12) and slower movements upslope (I3, I5) affecting depths up to 40 m. Landslide bodies C and C9 were identified as active parts of a multiple roto-translational slide. Time series from inclinometer I12, GPS S2, and piezometers at 15 and 36 m (P7) show concurrent seasonal cycles in piezometric levels and displacement rates, in phase with 180-day cumulative rainfall. This confirms the strong control exerted by seasonal weather patterns on medium- to deep-seated landslide activity.

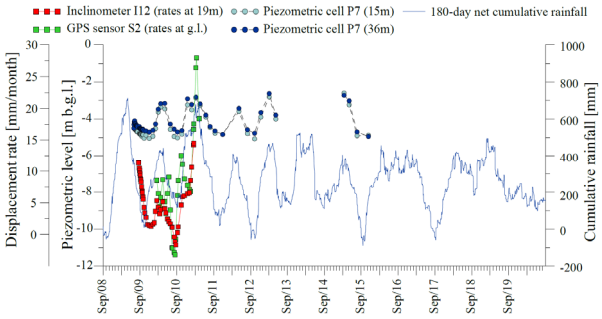

Figure 2. Pisciolo slope (modified from Cotecchia et al., 2014): 180-day cumulative rainfalls; piezometric heads at 36 m (Casagrande cell) and 15 m depth (electric cell) along P7 (z=0 at ground surface); displacement rates along the shear band at 19 m depth (I12) and at the ground surface (GPS S2). Data up to 2013 are from Cotecchia et al., (2014).

3 THE NUMERICAL MODELLING OF THE PISCIOLO SLOPE

Figure 3 shows the mesh for the 2D H-FE analyses, corresponding to section I–I' in Figure 1. Element sizes range from 0.25 m near the ground surface to 10 m at the model base, reproducing slope topography and hydraulic contrasts among the PD clays, fractured rocks/coarser strata, and topsoil. In the top 2 m, $k_{sat}=10^{-8}$ m/s, being one order higher than the 10^{-9} m/s set for the underlying PD fissured clays, to represent desiccation cracks increasing shallow permeability (Tagarelli et al., 2023). The PD clay water retention curve (WRC), derived from drying–wetting tests on undisturbed REV-size samples (Pedone et al., 2022a,b) and calibrated with the van Genuchten (1980) model. Fractured rock inclusions were found to remain saturated in sensitivity analyses and were modelled as fully saturated.

Steady-state seepage was first computed to initialize pore-water pressures, using boundary conditions in Figure 3: null pressure at the river valley floor, hydrostatic upstream boundary, impervious downstream and bottom boundaries, and free drainage along the slope. This yielded a summer-season suction of ~50 kPa along the surface. Transient seepage was then run for 2001–2020, implementing soil–vegetation–atmosphere (SVA) interaction via positive infiltration R(t) at the top boundary and negative evaporation E(t) and transpiration T(t) fluxes at shallow depths (Figure 4). E(t) and T(t) were estimated with the FAO Penman–Monteith method (Allen et al., 1998) using a dual crop coefficient approach, adjusted for vegetation cover, phenology, and bare-soil fraction, as follows:

$$E(t) = ET_0 * K_e \quad (1)$$

$$T(t) = ET_0 * K_{cb} \quad (2)$$

where ET_0 is the reference evapotranspiration; K_e the evaporation coefficient (Allen et al. 2008) implementing the area of bare topsoil across the slope ground surface; K_{cb} the transpiration coefficient, accounting for the plant type, growth stages during the year (Allen et al. 2008) and the percentage of vegetated surface. Details on the procedure to compute E(t) and T(t) have been reported by Tagarelli & Cotecchia (2025).

Both E(t) and T(t) were applied to nodes below the ground surface (inset of Figure 3), since only one flow function can be assigned per node. E(t) was applied at 0.05 m depth, while T(t) was applied at 0.25 m depth, assuming a triangular root-water uptake (RWU) distribution with maximum at the surface and zero at 0.75 m depth, consistent with the root depth of the local winter wheat (Allen et al., 1998).

Soil suction limits water uptake, as water with low potential energy (s > 0) is strongly bound to the soil skeleton and less available for extraction (Allen et al., 1998). This water stress effect (Feddes, 1982) was incorporated by scaling K_e and K_{cb} with reduction functions K_r and K_s, as follow:

$$E(t)_{adj} = ET_0 * K_e * K_r \quad (3)$$

$$T(t)_{adj} = ET_0 * K_{cb} * K_s \quad (4)$$

K_r and K_s (Allen et al., 1998) were implemented via the GeoStudio hydraulic modifier (GeoStudio, 2012) and are unity up to suctions of 300 kPa and 359 kPa, respectively, decreasing linearly thereafter and reaching zero at the wilting point (1500 kPa).

The present SVA simulation—including the computation of Inf(t), E(t), and T(t), and their spatial distribution in the mesh—is novel compared with previous SLVA modelling for the Pisciolo slope. Figure 4 reports the daily R(t), E(t), and T(t) fluxes (unadjusted, as K_r and K_s depend on the evolving suction s(t) computed in the model) over the 19-year period, using climatic data from a station 3 km from the slope.

The pore-pressure fields across the slope, $h(t)_{x,y}$ obtained from the H analyses were subsequently used in LE analyses (Morgenstern & Price, 1965) to compute $SF(t)_i$ for the pre-existing sliding bodies C9 and C (Figure 1). The shear strength parameters adopted for the computation of the SF(t) for bodies C9 and C correspond to those obtained thought back-analyses conducted in the past by Cotecchia et al., (2019).

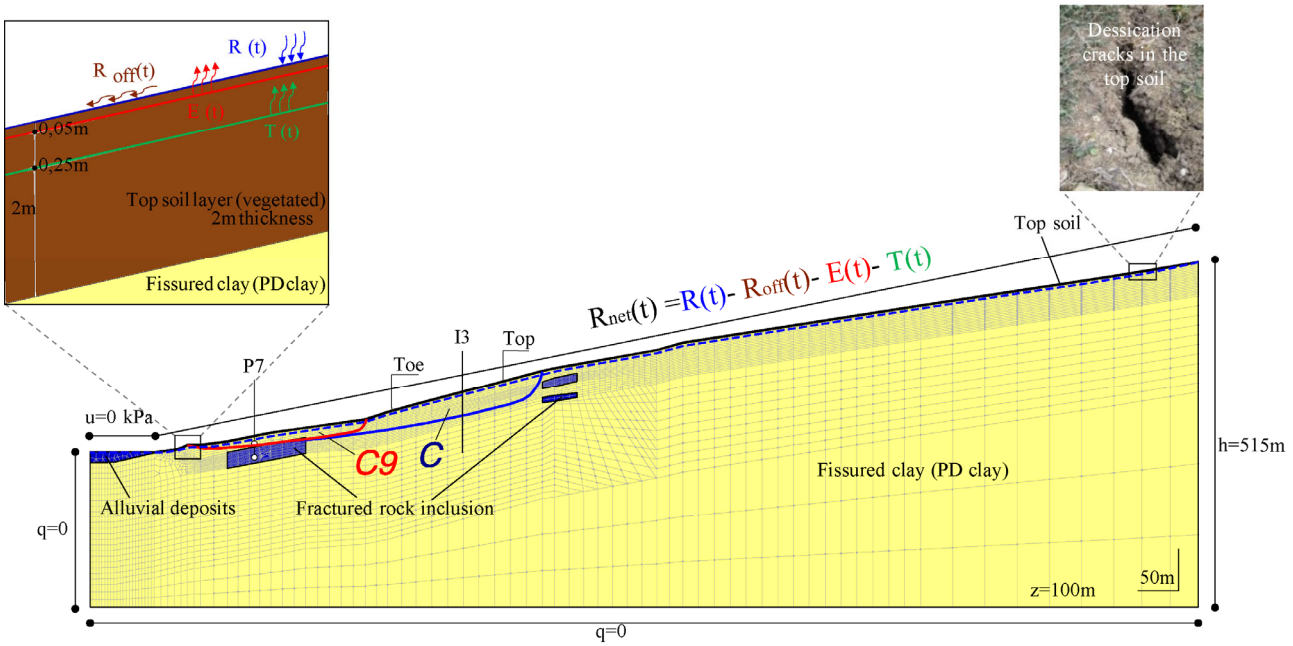

Figure 3. FE slope model and boundary conditions (section I-I' in Figure 1). The dashed line is the water table result of the steady-state analysis.

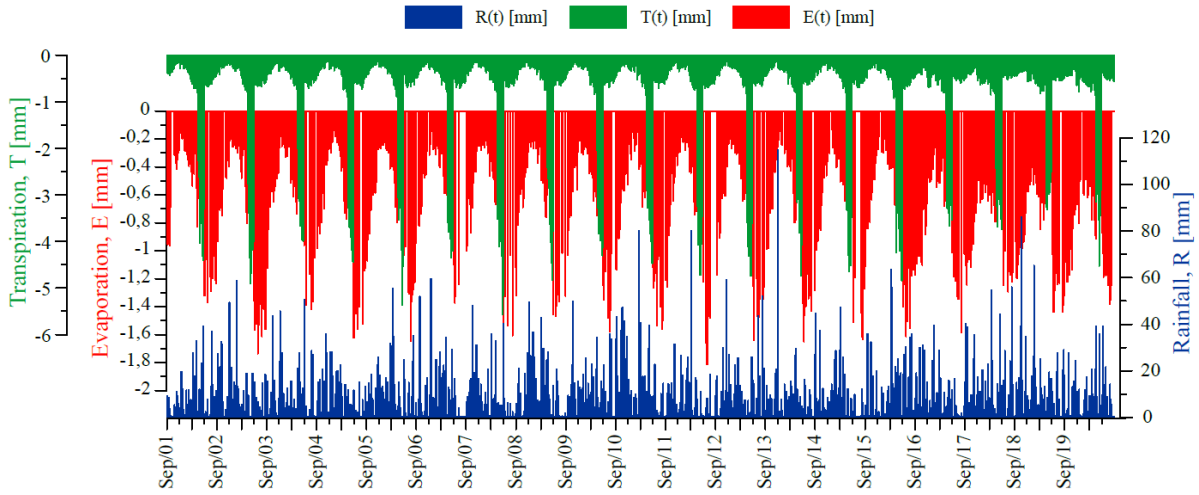

Figure 4. R(t), E(t), T(t) and atmospheric temperature from 1st September 2001 to 31st August 2020; the temperature, input for both the evaporation and transpiration computation, and the rainfall have been recorded at Melfi meteorological station.

4 THE WEATHER-INDUCED VARIATIONS IN PIEZOMETRIC HEAD

Figure 5 reports both the predicted and the monitored $h(t)_{15m}$ and $h(t)_{36m}$ along vertical P7 (Figure 1). Both $h(t)_{15m}$ and $h(t)_{36m}$ (dotted and dashed lines in Figure 5) are in very good agreement with the monitored piezometric heads (circles and crosses in Figure 5) in the period 2009-2015, since both the absolute values and the fluctuations over time are matched successfully. This agreement strongly supports the reliability of the adopted modelling procedure, despite its uncoupled nature. In particular, despite the evapotranspiration rates have been computed through a traditional semi-empirical approach like the FAO Penman-Monteith method, and the Roff has been dealt with through an automated routine, the success of the $h(t)_{x,y}$ predictions suggests that both these processing strategies provide sufficiently good estimates of ET and R_{off}, respectively. The piezometric head, h(t), is found to undergo variations concurring with long term $CumR_{net}$, i.e. $CumR_{net\text{-}180d}$ at large depth, and not to be affected by any single rainfall event, even when h(t) is maximum during the year. At both 15m and 36m depth, h(t) undergoes seasonal fluctuations as long as the weather conditions give rise to seasonal fluctuations of the $CumR_{net\text{-}180d}$.

Furthermore, the model predictions provide full evidence of the change in the h(t) pattern when a change in the yearly climatic pattern occurs. Indeed, from the start of winter 2015 to the end of 2020 (shaded portion of the plot, Figure 5), the distribution of the rainy days over the year has been different from the previous years (more rainy summers and drier winters), and both the E(t) and T(t) patterns have changed too. The numerical results show how, overall, such changes determine lower peak values of the piezometric heads with respect to those reached in the years characterized by seasonal fluctuations of $CumR_{net\text{-}180d}$. The peak in h(t) may be even shifted in time during the year, i.e. not correspond to the end of winter. It is worth highlighting, though, that although the $CumR_{net\text{-}180d}$ in 2015-2020 does not follow clear seasonal fluctuations, both the predicted $h(t)_{15m}$ and $h(t)_{36m}$ still undergo seasonal fluctuations which, though, as said before, are of far smaller amplitude than in the previous years (i.e., lower peaks and higher troughs).

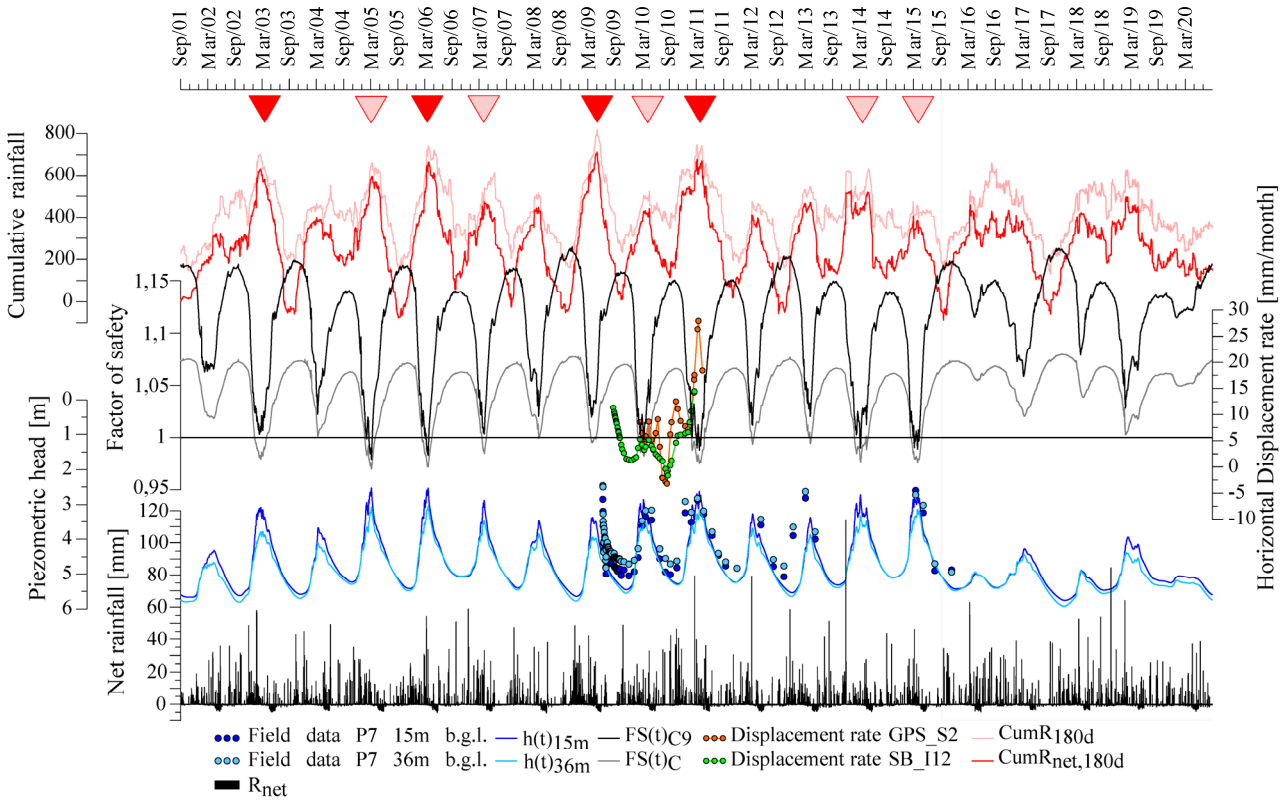

Figure 5. 1st September 2001 to 31st August 2020: R_{net}, $CumR_{180d}$, $CumR_{net\text{-}180d}$, computed and monitored $h(t)_{15m}$ and $h(t)_{36m}$ (zero head at ground level) along P7, together with both $SF(t)_{C9}$ and $SF(t)_C$. The displacement rate logged at the toe area of the bodies C and C9 at the ground level and along the inclinometer vertical I12 at the depth of the shear band are also reported.

5 THE WEATHER-INDUCED LANDSLIDE ACTIVITY

Figure 5 shows SF(t) predicted for both body C9 and body C (Figure 1 and 3) over 2001-2020. These predictions show that, for the "Mediterranean subcontinental to continental, partly semiarid to arid" climate (M4 type) like that at Pisciolo, SF(t) of deep bodies in clayey slopes increases monotonically from mid-April until December and reduces in winter, causing the reach of the minimum SF(t) typically in early spring, for those years characterized by seasonal fluctuations of $CumR_{net\text{-}180d}$, as previously reported by Pedone et al., (2018) and Cotecchia et al., (2019) running the analyses for a repetitive yearly $R_{net}(t)$.

In addition, the predictions in Figure 5 show that SF(t) still corresponds to $CumR_{net\text{-}180d}$ when a sequence of different hydrological years affects the slope equilibrium and the extent to which the yearly weather variability can determine a variability of the yearly SF(t) of the deep bodies. It follows that $CumR_{net\text{-}180d}$ is a weather function which relates successfully with both $SF(t)_{C9}$ and $SF(t)_C$ in general.

At the same time, the numerical predictions in Figure 5 show that $h(t)_{15m}$ and $h(t)_{36m}$ are powerful indicators of medium depth and deep landslide mobilization, respectively.

The numerical predictions in Figure 5 provide also indications about the reactivation mechanism for the deep landslide bodies at Pisciolo. They show that the deeper and

larger body C reaches instability, $SF(t)_C=1$, more often than body C9, which, on its own, undergoes larger weather-related excursions in stability (i.e. variations of $SF(t)_{C9}$) than body C, but with $SF(t)_{C9}$ reaching 1 less often. However, since body C9 is nested at the base of body C, when $SF(t)_C=1$ also body C9 moves.

Figure 5 also reports the horizontal displacement rates monitored along the shear band confining both bodies at the toe, as measured through inclinometer I12, and the displacement rate measured at the ground surface through the GPS sensor S2 (Figures 1 and 3). The figure makes evident how the predicted piezometric fluctuations, whose successful agreement with field data has been commented before, concur with the seasonal variations in displacement rate of both bodies C and C9 logged in situ, which in turn are in agreement with the predicted excursions of SF(t) in the monitoring period, 2009-2011. When the displacement rate reduces (reaching zero in July-August 2010), $SF(t)\geq1$ and reaches the peak value in July-August. Conversely, when the displacement rates are maximum (in March 2010 and March 2011), $SF(t)=1$. Furthermore, Figure 5 reports with arrows the timing of nine events of reactivation of both bodies C and C9, all taking place at the end of winter - early spring. These reactivations were recorded either due to the breakage of the aqueduct pipeline crossing the base of both bodies C9 and C (full arrows), or through field surveys, during which geomorphological evidence of recent landslide movements was logged (empty arrows). All these records of landslide activity are in good agreement with the predictions of $SF(t)_C=1$. For the remaining years in which the numerical results predict $SF(t)_C\leq1$, reactivation records are not available due to a lack of monitoring, but it cannot be excluded that landslide activity occurred.

The change in $CumR_{net\text{-}180d}$ pattern after 2015, thoroughly commented before, is found to bring about a mitigation of the activity of both the deep bodies C9 and C, with $SF(t)_C>1$ and $SF(t)_{C9}>1$ in all these years, except for $SF(t)_C=1$ in February 2019.

6 USE OF SLVA MODELLING TO INFORM SITE SCALE LEWS

The validation of the numerical predictions against field monitoring data discussed above, proves that the proposed modelling procedure of the SLVA interaction can be employed in the design of site scale LEWS. The proposed H-LE modelling can be continuously run, for any possible landslide body (of different extension and depth), accounting for weather now-casting, in order to forecast accelerations of landslide movements (i.e. the reach of $SF(t)=1$) and mitigate the risk.

The numerical data have confirmed $h(t)_{i,x,y}$ along the slip surface i to be the main indicator of $SF(t)_i=1$, for any landslide depth. It is worth highlighting, though, that if the LEWS is designed to relate the alert to real time monitoring of $h(t)_{i,x,y}$, it is not sufficient to monitor h(t) in a single point of the slip surface i, since the alert should be set for all the different $h(t)_i$ distributions along the slip surface corresponding to the reach of $SF(t)_i=1$. Therefore, the LEWS should be designed to monitor $h(t)_i$ at several points along the slip surface in the field, in order to issue the alert when the threshold $h(t)_{i,x,y}$ distribution corresponding to $SF(t)_i=1$ is monitored.

For deep landslides, such as bodies C9 and C, the modelling results have shed light on a robust correspondence between the SF(t) and $CumR_{net}$ over time lapses increasing with the depth of the slip surface, typically 6 months. Hence, the results suggest the use of weather functions like $CumR_{net\text{-}nd}$, for n about 180, in the definition of the precursor of these landslide reactivations, based upon numerical analyses inputting variable weather datasets.

An attempt to characterize the weather precursor for both landslides C and C9 has been carried based upon the numerical predictions in Figure 5. In particular, it has been recognized that the reach of either $SF_C=1$, or $SF_{C9}=1$, depends not only on the peak value of $CumR_{net\text{-}180d}$, but also on the weather regime in the dry period of the year and on the shape of the whole $CumR_{net\text{-}180d}$ yearly pattern. Therefore, the definition of the weather precursor for either bodies has been based on two functions: f.1) the minimum value of the $CumR_{net\text{-}180d}$ reached in the "dry period" (defined as the period of the year during which $CumR_{net\text{-}180d}$ decreases to the minimum value, usually occurring around September-November); f.2) the average gradient of $CumR_{net\text{-}180d}$ computed over the "wet period" (defined as the period of the year during which $CumR_{net\text{-}180d}$ increases from the minimum to the peak value, usually occurring around March-April). The function f.1 has been selected to account for the piezometric conditions in the slope before the season of major cumulative infiltration, whereas f.2 has been selected to account for the mean R_{net} in the wet period.

Figure 6 reports twice the plot f.1 vs f.2 over the period 2001-2020, where in Figure 6a each circle (corresponding to a single year) is grey when $SF(t)_{C9}\leq1$ and black when $SF(t)_{C9}>1$ and the same selection of colours applies to $SF(t)_C$ in Figure 6b. In both Figures 6a and 6b full circles correspond to the f.1 and f.2 calculated with reference to the $CumR_{net\text{-}180d}$, whereas empty circles correspond to the f.1 and f.2 computed with reference to the $CumR_{180d}$.

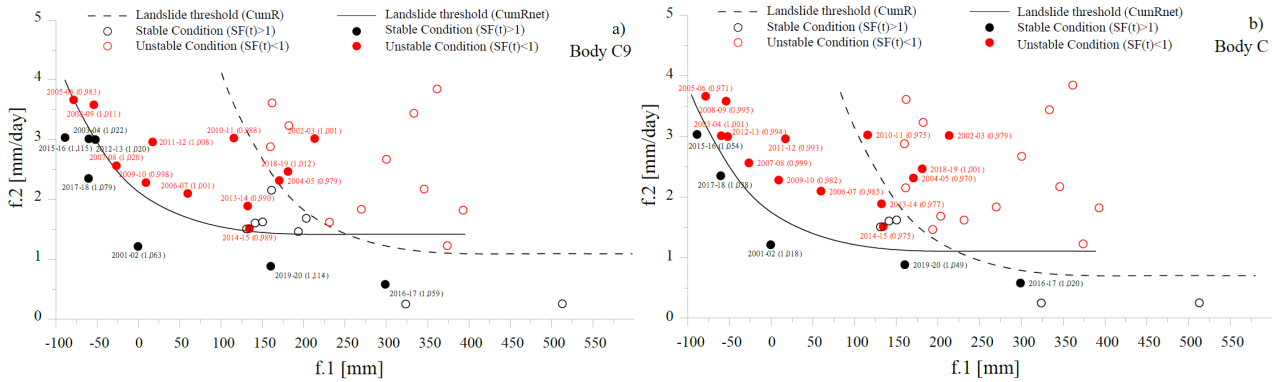

Figure 6. Average rainfall intensity - minimum 180-day net (empty symbols) and total (full symbols) cumulative rainfall data for Body C9 (a) and for Body C (b), together with a proposed threshold for the reactivation of deep landsliding at Pisciolo. In both plots the labels reporting the corresponding year and the SF, in the brackets, are reported only with reference to data referring to the net weather function.

The plots in Figures 6a and 6b then represent stability charts for the Bodies C9 and C, respectively, giving evidence to the existence of a function separating the portion of the chart corresponding to weather conditions determining SF(t)>1 over the whole year and that corresponding to the reach of SF(t)≤1. The two portions are separated by a continuous line, when making reference to the $CumR_{net\text{-}180d}$, and by a dashed line when making reference to the $CumR_{180d}$. Both lines represent weather precursor functions of the reactivation of landslide bodies C9 and C, and can be of use as threshold function for the weather-induced reactivation at Pisciolo.

7 CONCLUSIONS

The proposed deterministic H–LE modelling procedure successfully reproduced SLVA interactions controlling deep landslides at the Pisciolo slope, a representative case of unstable slopes in the south-eastern Apennines. Applied to 19 years of real weather data (2001–2020), the analyses quantified the effects on the piezometric regime, $h(t)_{x,y}$, and the safety factor evolution, SF(t)i, for the landslide bodies C9 and C. Agreement with field and monitoring data demonstrates its readiness for integration into site-scale LEWS and its broader applicability to other GHM contexts.

Piezometric head along the slip surface proved to be a reliable indicator of instability ($SF(t)_i \leq 1$) for the landslide bodies, provided it is monitored at multiple points. The study also provided a preliminary precursor function for deep landslides (bodies C and C9), with stability charts provided.

LEWS reliability could be enhanced by parametric SF(t) analyses using statistical weather scenarios to refine the $CumR_{net\text{-}nd}$–$SF(t)_i$ relation. While further improvements are expected from more advanced coupled HM/TH/THM modelling, the results support a paradigm shift in LEWS design—rooted in the specific landslide mechanism diagnosis. The procedure is also suited to assess climate change impacts on future slope stability.

ACKNOWLEDGEMENTS

The authors are grateful for the financial support provided by the project PNRR, MISURA M4_C2_1.4, National Centre for HPC, Big Data and Quantum Computing (CN_00000013) - Spoke 5 “Environment and Natural Disasters”.

REFERENCES

Allen, R. G., Pereira, L. S., Raes, D., & Smith, M. (1998). Crop evapotranspiration-Guidelines for computing crop water requirements-FAO Irrigation and drainage paper 56. Fao, Rome, 300(9), D05109.

Blight, G. (1997). Interactions between the atmosphere and the Earth. Geotechnique.

Calvello, M., d’Orsi, R. N., Piciullo, L., Paes, N., Magalhaes, M., & Lacerda, W. A. (2015). The Rio de Janeiro early warning system for rainfall-induced landslides: analysis of performance for the years 2010–2013. International journal of disaster risk reduction, 12, 3-15.

Cecconi, M., Tagarelli, V., Cotecchia, F., Pane, V., Anselmucci, F., Bertolini, I., Biondi, G., Boldrin, D., Capobianco, V., Cardile, G. and Cuomo, S., 2025. Soil-vegetation-atmosphere interaction for engineering applications: recent multi-scale and multi-disciplinary insights. Geomechanics for Energy and the Environment, p.100723.

Cotecchia, F., Pedone, G., Bottiglieri, O., Santaloia, F., & Vitone, C. (2014). Slope-atmosphere interaction in a tectonized clayey slope: A case study. Rivista Italiana Di Geotecnica, 48(1), 34–61.

Cotecchia, F., Tagarelli, V., Pedone, G., Ruggieri, G., Guglielmi, S., & Santaloia, F. (2019). Analysis of climate-driven processes in clayey slopes for early warning system design. Proceedings of the Institution of Civil Engineers: Geotechnical Engineering, 172(6), 465–480. https://doi.org/10.1680/JGEEN.18.00217

Elia, G., Cotecchia, F., Pedone, G., Vaunat, J., Vardon, P. J., Pereira, C., Springman, S. M., Rouainia, M., Van Esch, J., Koda, E., Josifovski, J., Nocilla, A., Askarinejad, A., Stirling, R., Helm, P., Lollino, P., & Osinski, P. (2017). Numerical modelling of slope-vegetation-atmosphere interaction: An overview. Quarterly Journal of Engineering Geology and Hydrogeology, 50(3), 249–270. https://doi.org/10.1144/QJEGH2016-079

Feddes, R. A. (1982). Simulation of field water use and crop yield (pp. 194–209). Pudoc. https://research.wur.nl/en/publications/simulation-of-field-water-use-and-crop-yield

Gariano, S. L., Brunetti, M. T., Iovine, G., Melillo, M., Peruccacci, S., Terranova, O., Vennari, C., & Guzzetti, F. (2015). Calibration and validation of rainfall thresholds for shallow landslide forecasting in Sicily, southern Italy. Geomorphology, 228, 653–665. https://doi.org/10.1016/J.GEOMORPH.2014.10.019

Gens A., (2010) Soil–environment interactions in geotechnical engineering. Géotechnique 60(1): 3–74, https://doi.org/10.1680/geot.9.P.109

GeoStudio reference manual (2012).

Morgenstern, N. R., & Price, V. E. (1965). The analysis of the stability of general slip surfaces. Geotechnique, 15(1), 79–93. https://doi.org/10.1680/GEOT.1965.15.1.79

Oorthuis, R., Hürlimann, M., Fraccica, A., Lloret, A., Moya, J., Puig-Polo, C., & Vaunat, J. (2018). Monitoring of a full-scale embankment experiment regarding soil–vegetation–atmosphere interactions. Water, 10(6), 688.

Pedone, G., Cotecchia, F., Tagarelli, V., Bottiglieri, O., & Murthy, M. B. N. (2022b). An Investigation into the Water Retention Behaviour of an Unsaturated Natural Fissured Clay. Applied Sciences 2022, Vol. 12, Page 9533, 12(19), 9533. https://doi.org/10.3390/APP12199533

Pedone, G., Ruggieri, G., & Trizzino, R. (2018). Characterisation of climatic variables used to identify instability thresholds in clay slopes. Geotechnique Letters, 8(3), 231–239. https://doi.org/10.1680/JGELE.18.00020

Pedone, G., Tsiampousi, A., Cotecchia, F., & Zdravkovic, L. (2022a). Coupled hydro-mechanical modelling of soil–vegetation–atmosphere interaction in natural clay slopes. Https://Doi.Org/10.1139/Cgj-2020-0479, 59(2), 272–290. https://doi.org/10.1139/CGJ-2020-0479

Rianna, G., Reder, A., & Pagano, L. (2023a). From empirically to physically based early warning predictions of rainfall-induced landslides in silty volcanic soils: the Lattari Mountains case study. Bulletin of Engineering Geology and the Environment, 82(6), 1–20. https://doi.org/10.1007/S10064-023-03228-X/TABLES/3

Salciarini, D., Tamagnini, C., Conversini, P., & Rapinesi, S. (2012). Spatially distributed rainfall thresholds for the initiation of shallow landslides. Natural Hazards, 61(1), 229–245. https://doi.org/10.1007/S11069-011-9739-2/FIGURES/11

Tagarelli, V. and Cotecchia, F., 2025. Weather-Induced Landslide Activity in Clayey Slopes: Modeling for the Design of Site-Scale Early Warning Systems. Journal of Geotechnical and Geoenvironmental Engineering, 151(9), p.04025092.

Tagarelli, V., & Cotecchia, F. (2022). Preliminary field data of selected deep-rooted vegetation effects on the slope-vegetation-atmosphere interaction: results from an in-situ test. Rivista Italiana Di Geotecnica, 56(1), 62–83. https://doi.org/10.19199/2022.1.0557-1405.062

Tagarelli, V., Stasi, N., & Cotecchia, F. (2023). Numerical Back-Analysis of In-Situ Constant Head Tests in Partially Saturated Soil Cover to Determine the Permeability Function. In National Conference of the Researchers of Geotechnical Engineering (pp. 275-282). Cham: Springer Nature Switzerland.

Van Genuchten, M. (1980). A closed-form equation for predicting the hydraulic conductivity of unsaturated soils. Soil Sci Soc Am J, 44, 892–898.